NOAA Technical Memorandum ERL WPL-129

CLOUD BASE HEIGHTS FROM LIDAR, ROTATING BEAM CEILOMETER, AND PILOT REPORTS COMPARED BY EXPERIMENT AND THEORY

W. L. Eberhard

Wave Propagation Laboratory
Boulder, Colorado
January 1986

noaa NATIONAL OCEANIC AND ATMOSPHERIC ADMINISTRATION / Environmental Research Laboratories

NOAA Technical Memorandum ERL WPL-129

CLOUD BASE HEIGHTS FROM LIDAR, ROTATING BEAM CEILOMETER, AND PILOT REPORTS COMPARED BY EXPERIMENT AND THEORY

W. L. Eberhard

Wave Propagation Laboratory
Boulder, Colorado
January 1986

UNITED STATES
DEPARTMENT OF COMMERCE

Malcolm Baldrige,
Secretary

NATIONAL OCEANIC AND
ATMOSPHERIC ADMINISTRATION

Anthony J. Calio,
Administrator

Environmental Research
Laboratories

Vernon E. Derr,
Director

NOTICE

Mention of a commercial company or product does not constitute an endorsement by NOAA Environmental Research Laboratories. Use for publicity or advertising purposes of information from this publication concerning proprietary products or the tests of such products is not authorized.

CONTENTS

CLOUD BASE HEIGHTS FROM LIDAR, ROTATING BEAM CEILOMETER, AND PILOT REPORTS COMPARED BY EXPERIMENT AND THEORY

W. L. Eberhard
NOAA/ERL/Wave Propagation Laboratory
Boulder, Colorado 80303

ABSTRACT. An experiment is described, wherein cloud signals from a range-corrected ruby lidar and a rotating beam ceilometer showed excellent agreement in height at which peak signal occurred. However, pilot reports of ceiling when viewing at 3° below horizontal were at significantly lower altitude. To develop an understanding of the relationships between ceilometer signals and pilot visibility, the physical bases of these signals and of pilot's perceptions are analyzed. A relationship is derived that connects pilot optical depth with an idealized lidar's signal profile by applying reasonable approximations to the cloud structure (with or without precipitation). The view angle of the pilot, the lidar's pointing direction, and the vertical distribution of the obscuring particles control the relationship. This relationship is recommended as the foundation of a signal-processing algorithm for better ceiling measurements. Multiple scattering and a ceilometer's range dependence and resolution are complicating factors. Accurate cloud base predictions should also account for horizontal inhomogeneities at the cloud's bottom as shown by simple examples. All of these concepts are also pertinent to measurement of slant visual range. A monitoring program to study the variation of optical density near cloud bottom, especially during low ceiling or when accompanied by precipitation, is needed to improve ceilometer practice.

1. INTRODUCTION

Obscuration of a pilot's view by clouds, fog, and precipitation is an important consideration in aviation operations and safety. Ground-based instruments such as cloud height sensors and transmissometers attempt to measure the type and severity of the obscuration in order to advise pilots and air traffic controllers. Improvements in the accuracy and completeness of these types of measurements would probably increase safety and reduce the cost of aviation operations. Research activities have made some progress in developing a method to measure slant visual range (e.g., Gaumet and Petitpa, 1982; Viezee et al., 1969).

As part of an effort to improve the cloud ceiling measurements, the National Weather Service (NWS) asked the Wave Propagation Laboratory (WPL) to compare signals from a rotating beam ceilometer (RBC) and a lidar operated as

a ceilometer, and to attempt to relate these signals to the optical depth experienced by a pilot. Eberhard et al. (1980) reported some preliminary results. A better understanding of these relationships, perhaps in combination with the application of modern optical and signal processing technologies, may lead to a significant increase in value of the cloud reports for the aviation industry.

NWS has traditionally defined cloud base height (CBH) as the height at which the RBC signal reaches its maximum value. This definition is apparently founded on a simple model of a homogeneous cloud with clear air beneath. As the Rotating Beam Ceilometer System Instruction Manual (1967) explains, the signal is zero from all points below the cloud and is attenuated from points deep within the cloud, leading to a signal peak at the cloud's bottom edge. At least some of the available evidence argues that this is a poor choice. In the first place, density at cloud bottom usually increases continuously in the vertical, albeit sharply at times. For example, the careful measurements of Noonkester (1984) on marine stratus show a gradual increase. Such gradients make the physical significance of the peak signal uncertain. More direct evidence against using the height for peak signal comes from Eggert (1960), who reported substantial differences between CBH from the RBC and pilot reports of altitude upon acquiring visual contact during normal 3° glide slope approaches to an airport when cloud bases were lower than about 240 m (800 feet). His linear regression analysis revealed that when the RBC ceiling changed by ΔH the pilot's reporting altitude increased on average by only 0.55 ΔH rather than the ideal 1.00 ΔH. An additional nonscientific but thought-provoking piece of evidence was offered by a tower controller. He considers the onset of the RBC signal below the peak to be a more dependable choice than the peak, and normally reports accordingly rather than using the official NWS definition. In response to these doubts about the wisdom of using the location of peak signal for defining cloud base, this paper proposes an improved method for interpreting ceilometer signals. Not all issues are resolved, but the important factors, some of which have been largely ignored in the past, are discussed.

Although this work is mainly concerned with measurement of clouds with relatively distinct bottom edges, part of the discussion applies to low-

altitude obscuration, where a direct measure of slant visual range is desirable. The present development differs from related efforts on slant visual range by emphasizing a cloud sensor that points vertically (more or less) rather than at a low angle, such as up a glide slope of 3° or even opposite a cockpit cut-off angle of nominally 15°.

Three phrases are used with similar but distinct meanings. "Cloud base height" refers to the distance above the surface as reported by a ceilometer according to an objective criterion placed on the signal, such as height for the RBC's peak signal. "Cloud bottom" means the general vicinity of the lower portion of a cloud where obscuration is significant. "Cloud fringe" is the lowest extent of a cloud in a mathematical model.

2. EXPERIMENTAL COMPARISON OF LIDAR, ROTATING BEAM CEILOMETER, AND PILOT REPORTS

A research lidar system and RBC were operated side-by-side in order to compare their signals from cloud. On two occasions during these measurements a pilot flew a sequence of alternating ascents and descents near the ceilometers and reported the altitude from the pressure altimeter upon losing or gaining visual contact with the surface. The first objective of the experiment was to determine any difference between lidar and RBC measurements of the height to the base of the cloud. A second objective was to evaluate how the pilot's report of ceiling height was related to the signal acquired by each ceilometer technique.

2.1 Experiment Design

The experiment included several precautions designed to minimize the effects of natural cloud variability. The official NWS interpretation of cloud base height for the RBC was applied, namely the height for maximum signal. Since this is a very simple feature to identify, the same definition was applied to the lidar data after correction for the geometrical range dependence. The lidar was positioned only 5 m from the RBC receiver in order to minimize differences due to horizontal variations in cloud cover. For the RBC-lidar comparison, data segments were selected during which the RBC

revealed constant height to cloud base. Each segment also exhibited uniform signal width, which indicated constant depth of penetration of the RBC's radiation during the segment. The experiment did not take place at an airport, where the pilot's flight pattern would have been hampered by airport operations. Instead we operated in a rural area, where the pilot could perform many passes through the bottom of the cloud near the ceilometers within a short period of time. Unfortunately the two measurement periods with pilot reports contained variations in cloud base height as great as ~100 m. Except for this one complication, these procedures highlighted any inherent differences between the lidar, RBC, and pilot visual experience by eliminating as much as possible any discrepancies introduced by spatial and temporal variation in cloud properties.

2.2 Lidar Operation

WPL's lidar is a versatile research instrument that has participated in a variety of measurement programs, including cloud studies (Derr et al., 1976; Lopez, 1977; Platt et al., 1978), profiling of the stratospheric aerosol layer (De Luisi et al., 1982), and plume tracking in atmospheric dispersion studies (Eberhard, 1983; Gudiksen et al., 1984). The lidar's optical and electronic characteristics are well understood, and in this experiment its signal profiles were recorded with better resolution and precision than the RBC's signals. The lidar data therefore became the standard for comparison.

The zenith-pointing lidar measured the height to cloud base by determining the round trip time of flight of a short light pulse scattered by the cloud particles. The transmitter was a pulsed ruby laser emitting at 694.3 nm wavelength with typically 0.8 J pulse energy. The full width divergence angle to the e^{-2} points was 1.0 mr (0.06°). The measured range resolution, including pulse width and receiver electronic response time, was 7 m full width at half maximum from a single target. The Newtonian receiving telescope with 6 mr (0.34°) field of view had a primary mirror of 70 cm diameter, which was much larger than necessary for these strong cloud signals. Absorbing filters in the receiver's optical path attenuated the backscatter to the appropriate level for the photomultiplier detector and data acquisition electronics. A narrow-band filter with 1.0 nm bandwidth removed most of the background light.

A fast analog-digital converter recorded the detector's output at range intervals of 1.5 m, except for the highest cloud reported here when the range interval was 3.0 m. A minicomputer recorded the profile of the received signal from each pulse on digital magnetic tape together with auxiliary information such as time, pointing angle, and pulse energy.

Since height to the cloud was of central importance in the experiment, every effort was made to assure range accuracy. The lidar system pretriggered the analog-digital converter, which recorded a zero range mark created by illuminating the detector with a small fraction of energy from the outgoing pulse. A fiber optic cable carried this light from the laser's output optics to the detector. Range was computed from the known speed of light by the time elapsed between the zero range mark and any desired point of the backscattered signal. A quartz-controlled oscillator in the analog-digital converter assured time measurements accurate to better than 1 part in 10^4. As a final step to ensure range accuracy, corrections for lidar height above the ground and optical path lengths within the lidar were applied during data reduction.

Cloud base height was later extracted from the lidar data by first correcting each pulse's profile for the lidar's geometrical range dependence. The height where peak signal occurred was determined for each pulse, and these heights were then averaged for all pulses included in the data segment.

2.3 RBC Operation

For this project the NWS lent an RBC with Gifft recorder to WPL that was like many others in use at airports throughout the United States. WPL personnel installed the RBC; an NWS technician checked it for proper operation once during the autumn of 1979 and again during the spring of 1980 and found no discrepancies. A pole leaning over the receiver and extending about 1 m above provided additional verification of RBC alignment by generating a signal near the correct height.

The RBC used optical triangulation to measure the height to cloud base (Fig. 1). The rotating transmitter swept a narrow beam of light in a vertical plane, which also included the vertically-viewing receiver. The strongest output signal was created during the transmitter sweep when the beam inter-

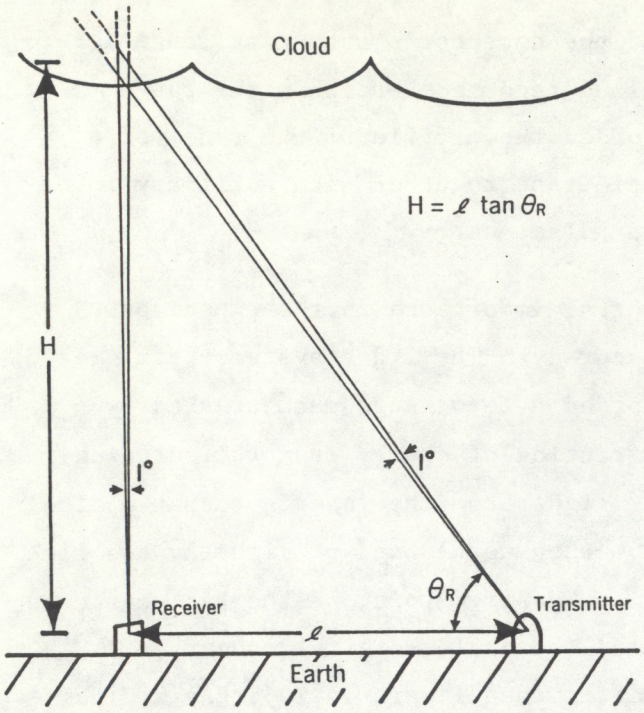

Figure 1.--RBC geometry for determining cloud base height by triangulation.

cepted the bottom of the cloud directly above the receiver. The height to this point was calculated from

$$H = \ell \tan\theta_R \ , \qquad (1)$$

where ℓ was the length of the baseline between transmitter and receiver, and θ_R was the transmitter's elevation angle for the strongest signal.

The transmitter consisted of a bright incandescent lamp at the focal point of a parabolic mirror of 61 cm diameter. Based on the dimensions of the double-coiled lamp filament, ray tracing showed that the transmitted beam was roughly trapezoidal in shape with 3.8° full divergence angle in the horizontal and 1.0° in the vertical plane. The transmitter unit rotated the lamp and mirror at constant angular velocity in the vertical plane.

The receiver was located at a baseline distance of 457 m (1500 feet), which was expected to produce the best resolution for typical cloud heights at the site north of Denver, Colorado. The receiver viewed vertically in the plane swept out by the transmitted beam with a lead sulfide detector at the focal point of a mirror that was identical to the transmitter mirror.

Unlike the laser, which emitted virtually monochromatic light, the RBC operated over a broad spectrum in the near infrared. The effects of background light were reduced in three ways. First, the transmitter and receiver each possessed a cover glass that transmitted infrared but absorbed visible wavelengths. The filtering on the transmitter prevented the bright light from annoying pilots or other persons in the vicinity. A band-pass filter next to the detector also restricted sensitivity to the infrared wavelengths. Second, the transmitted beam was modulated by a rotating shutter, and the detector output was passed through an electronic narrow-pass filter centered on the same frequency. The third feature was a metal honeycomb in the receiver for the purpose of reducing stray light. The system sensitivity as a function of wavelength was calculated from the spectral efficiencies of the various components. The source was assumed to be a black body at 3000 K, the manufacturers' specifications for the IR-transmitting cover glass and detector filter were applied, and a standard sensitivity curve for the lead sulfide detector was used. The resulting spectral response (Fig. 2) does not include losses due to molecular absorption, which can be significant in some bands in this wavelength region.

Without the honeycomb, ray tracing from the rectangular detector showed a trapezoidal-shaped receiver field with 5.6° divergence angle perpendicular to the swept plane and 0.9° in the direction parallel to the baseline. Ray tracing based on the dimensions of the honeycomb cells showed that the 0.9°

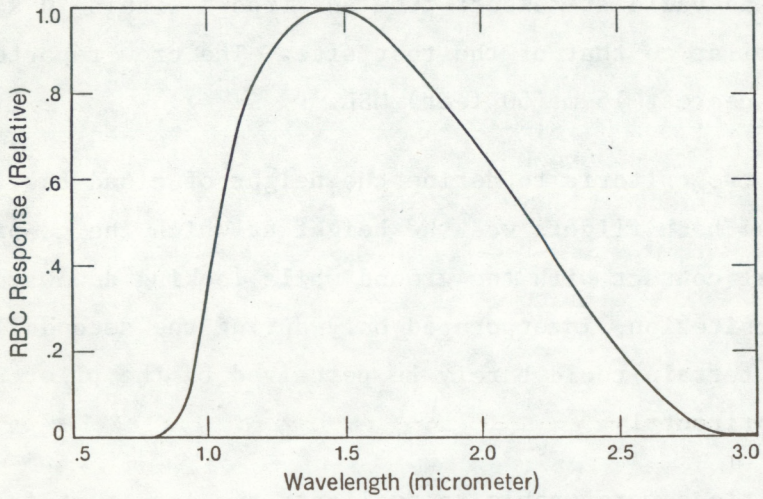

Figure 2.--Calculated spectral response of RBC.

angular dimension was unaffected, but the perpendicular dimension was reduced to roughly 3.7°.

After electronic amplification and filtering of the RBC signal, the Gifft recorder rectified it with a synchronous detector in phase with the modulating shutter. The facsimile recorder created a permanent graph of the signal profile, the strongest signal appearing darkest on the paper. The recorder also added angle and time marks to the record.

The RBC's version of cloud base height for each selected time segment was obtained by inspecting the facsimile record to find the RBC angle at maximum darkness or signal magnitude. When the dark region had a broad peak, the midpoint of the angles where the signal commenced its decrease was used. The angle was adjusted by the deviation of the pole's signal from its proper location a few feet above the receiver.

2.4 Pilot Reports

Two separate flights of a Cessna 205 supplied pilot reports of cloud base. The pilot flew back and forth above the ceilometers, using a nearby road to assist in orientation. Ascents and descents through cloud base were timed to occur as near the ceilometers as possible. A scientist, who was also an experienced amateur pilot, assisted with observations and recorded the altitudes at visual contact for each vertical transition. The pilot used an altimeter setting that was valid at takeoff from an airport within 20 km distance and at elevation similar to that of the test site. The crew reported cloud base heights to the nearest 15 m (50 feet) MSL.

The pilots used two criteria to define the height of cloud base. One criterion invoked during both flights was the height at which the co-pilot could barely achieve visual contact with the ground while looking downward near the nadir. The second criterion, incorporated only during the second flight, was the height at which terrain could barely be perceived by the pilot at a view angle of 3° below horizontal.

These test conditions were unable to duplicate one important factor normally encountered at an airport under similar low overcast. An airport's

bright approach lights would normally enable the pilot to attain visual contact at a higher altitude than if only the naturally lighted surface were available for visual orientation. In spite of this difference, the pilot's data demonstrate some important aspects of the ceiling measurement problem.

2.5 Results

The heights for maximum signal from the lidar and RBC were in close agreement. Eight data segments were selected according to the criteria of stable cloud signal recorded by the RBC and availability of concurrent lidar data. These events occurred on several different days with a variety of cloud heights. Lidar data were reduced after the selection was completed. Table 1 lists the results, ordered according to cloud height, and includes the differences between the two methods. The peak signals by the two methods occurred at virtually identical heights during some of the segments but deviated somewhat during others. The larger differences were approximately at the limits of experimental accuracy. Most of the potential for error lay with the RBC. The mercury switch that marks the 0° angle of the transmitter was difficult to position precisely; errors were estimated within the range of ±0.5°. The breadth of the cloud signal on the RBC record (Table 1) also lent some inaccuracy. Errors as large as 25% of this breadth are reasonable. In

Table 1. Cloud base measurements from lidar and RBC for selected stable periods

Date (mon/day/year)	Local begin time	Duration (minutes)	Lidar Height (m)	RBC Angle (°)	Difference (m)	Difference (°)	Breadth(°) of maximum RBC signal
4/23/80	1140	1.0	167	20.0	0.3	0.0	2
4/23/80	1221	3.0	249	28.6	-0.3	0.0	2
4/23/80	1453	2.0	367	39.0	-3.4	-0.2	1
11/ 5/79	1816	3.3	685	57.7	-38	-1.4	2
3/26/80	1357	2.0	1032	67.0	-45	-0.9	1 1/4
3/25/80	1508	1.5	1659	74.4	21	0.2	1
11/ 8/79	2151	3.0	1835	75.7	41	0.3	1 1/2
11/ 7/79	1211	3.0	3189	82.2	-148	-0.4	3/4

spite of the overlapping volumes viewed by the two devices, it is possible that spatial variations in the cloud contributed some minor differences due to the larger volume intercepted by the RBC. The data showed no bias between lidar and RBC heights for peak signal.

The aircraft encountered periods characterized by moderate variations in the height of cloud base, which required a different method for comparison. For each of the two periods when lidar, RBC, and pilot data were all available, time was partitioned into short segments 1/2 to 6 1/2 minutes long. The average RBC angle of maximum signal could be accurately determined for each segment, which was selected to exhibit little change in cloud height or else approximately linear change with time. Comparisons with lidar data were first performed for each partition, and then statistics were formed on the differences for the entire period. Statistics were also computed for the pilot reports. Table 2 lists the results for two flights on April 23, 1980.

In spite of the fluctuating cloud bottom, the two ceilometers showed almost identical heights for cloud base when averaged over each period. However, the rms difference of CBH between the lidar and RBC were considerably larger than the average difference. It is noteworthy that the real changes in cloud base, as indicated by the rms change in CBH by either sensor, were larger than the discrepancies between the two methods, which are indicated by

Table 2. Statistics of cloud base height (m) from lidar, RBC, and pilot reports

Parameter	Case 1	Case 2
Time (MST)	1130-1202	1458 1/2-1517
# Pilot reports	11	10
Cloud base heights:		
Average (lidar)	225.3	306.0
Average (RBC)	221.9	309.7
Average (pilot, downward)	229.2	312.4
Average (pilot, 3° depression)	-----	228.6
rms difference (lidar, RBC)	11.9	24.7
rms change (lidar)	27.7	32.0
rms change (RBC)	31.1	47.9
rms change (pilot, downward)	18.6	28.7
rms change (pilot, 3° depression)	-----	20.7

the rms difference. The agreement of the long-term average in the presence of significant differences for shorter segments suggests that proper interpretation of ceilometer signals from a nonuniform cloud bottom can be a greater problem than minor differences between sensing techniques.

Reports of cloud base from the pilot peering downward corresponded closely with the height for maximum signal from both the RBC and lidar. However, when looking forward at a 3° depression angle, the pilot on average reported visual contact at about 79 m (260 feet) below the height for maximum signal. During this test simulating a pilot viewing along his glide path, he therefore had to descend significantly lower than the average RBC or lidar CBH before acquiring visual contact. Further insight can be gained by examining the height of lowest observable RBC signal on the facsimile record. Although this parameter is a function of gain setting on the instrument, it does provide an upper limit on the location of the lowest part of the cloud. For Case 2 the lowest observable signal appeared at an average height of 273 m with an rms variation of 37 m. The pilot, viewing at 3° below horizontal, gave reports of visual contact that on average were even lower (at 229 m) than the average onset of RBC signal.

2.6 Discussion

The lidar and RBC measurements of cloud base heights of well-defined clouds with vertically stationary bottoms agreed within the experimental error. The criterion used was the height at which maximum signal was received. This result for ideal conditions provides encouragement that the range-corrected signal from a pulsed lidar ceilometer will produce results nearly identical to those of an RBC when the location of peak signal is the criterion for cloud base height.

The altitudes at which the pilot reported visual contact with the ground while looking downward agreed closely on average with the cloud base height measured by either the lidar or RBC. However, a disturbing result of the experiment was that the pilot looking forward, along a simulated glide slope as if searching for an airfield during instrument approach, had to descend an additional 84 m to 229 m altitude before achieving visual contact. This

finding casts doubt on the wisdom of using the height for peak signal as the criterion appropriate for aviation safety. Horizontal variations certainly must have contributed to this phenomenon, because any protrusions of cloud into the pilot's line of sight would have blocked his view of the surface.

The discrepancy prompted the thorough analytical evaluation of the relationship between ceilometer signals and pilot visibility that constitutes the remainder of this paper. It became apparent that measurements, oversimplified models of cloud structure, or even a combination thereof would be insufficient for determining this relationship.

3. ANALYTICAL EVALUATION OF CEILOMETER SIGNALS AND PILOT VISIBILITY

3.1 Idealized Equations of Radiative Transfer for Horizontally Homogeneous Clouds

In order to relate ceilometer signals to pilot visibility, idealized equations of radiative transfer are first written separately for the lidar, RBC, and pilot's view along his line of sight. Some nonideal factors that require consideration in a practical instrument are discussed in Section 3.3.

3.1.1 Lidar

The equation for signal strength from an ideal detector in a pulsed monostatic lidar can be expressed as

$$P_L(R) = K_L F_L(R) \beta_L(R) \exp\left[-2 \int_0^R \sigma_L(R')dR'\right] , \qquad (2)$$

where R is range along the pulse path, β_L is the backscatter coefficient, and σ_L is the extinction coefficient due to scattering and absorption. The time t for the round trip flight of the pulse to a target yields the range to that target according to $R = ct/2$, where c is the speed of light. The range resolution $\Delta R = c\tau/2$ is determined by the duration τ of signal from a point target. The equation for $P_L(R)$ assumes that $\Delta R \ll R$. The factor K_L includes system parameters (e.g., Viezee, et al., 1969), such as laser pulse energy, optical gathering power of the telescope, detector responsivity, and electro-

nic gain. The factor $F_L(R)$ describes the change in signal with range due to optical geometry. In the far field where the receiver field of view completely overlaps the outgoing pulse, $F_L(R) = R^{-2}$. Close to the lidar $F_L(R)$ becomes smaller than R^{-2} because of partial overlap of the outgoing pulse with the field of view and poor focus of the receiver. The expression for $P_L(R)$ assumes single scattering (see Section 3.3.5).

The most obvious pointing direction for a lidar ceilometer is toward the zenith, where R = z. However, some advantage might be gained by aiming the lidar at another elevation angle θ_L, such as up the approach path of the active runway. In this case the height where backscatter occurs is

$$z = R \sin\theta_L \ . \tag{3}$$

By assuming that the clouds are horizontally homogeneous and correcting the signal for the system parameters, we can define a range-corrected signal shape function

$$b_L(z) = \frac{P_L(z/\sin\theta_L)}{K_L \, F_L(z/\sin\theta_L)} \tag{4}$$

or

$$b_L(z) = \beta_L(z) \exp\left[-\frac{2}{\sin\theta_L} \int_0^z \sigma_L(z')dz'\right] . \tag{5}$$

If the lidar is calibrated, b_L gives the profile of the backscatter coefficient as modified by extinction in the intervening medium. Even in the absence of a calibration, this relation for the range-corrected shape of the profile is compared below with similar expressions for the RBC and the pilot's optical depth.

3.1.2 Rotating beam ceilometer

The equation for RBC signal strength $P_R(z)$ is like that for the lidar, except that the light takes a different path, the scattering is at an angle between 90° and 180°, and the optical geometry factor has a different form. For the horizontally homogeneous cloud and single scattering we have

$$P_R(\theta_R) = K_R F_R(\theta_R)\beta_R(z,\theta_R) \exp\left[-\frac{1}{\sin\theta_R}\int_0^z \sigma_R(z')dz'\right] \times \exp\left[-\int_0^z \sigma_R(z')dz'\right], \quad (6)$$

where K_R is the system constant. The Appendix discusses the form of the optical geometry factor $F_R(\theta_R)$. The first exponential in (6) describes the extinction of the radiation between the transmitter and the scattering point, which lies within the volume intersected by transmitter and receiver. The second exponential accounts for extinction between the scattering point and the receiver. Identical values of the extinction coefficient $\sigma_R(z)$ in the exponents imply attenuation that is independent of direction. The single-scattering cross-section β_R is a function of the height and also the scattering angle, the latter in turn depending on the RBC angle θ_R. Since the cloud return for each sweep is usually limited to a small range of values for θ_R, namely $\Delta\theta_R \lesssim 20°$, we can substitute the characteristic value $\bar{\theta}_R$ in the equation for P_R.

The RBC equation can then be formulated as

$$b_R(z) = \frac{P_R(\bar{\theta}_R)}{K_R\, F_R(\bar{\theta}_R)}$$

$$= \beta_R\,(z,\bar{\theta}_R) \exp\left[-\left(1 + \frac{1}{\sin\bar{\theta}_R}\right)\int_0^z \sigma_R(z')dz'\right], \quad (7)$$

which is very similar to the analogous expression for the lidar. Normalization of the lidar data by $K_L\, F_L(R)$ is a common procedure, but the RBC signal is displayed without such normalization. However, it is shown in the Appendix that $K_R\, F_R(\theta_R)$ can often be assumed constant over the interval of significant cloud return, allowing us to use

$$b_R(z) \simeq \text{constant} \times P_R(z)$$

for the profile shape.

3.1.3 Pilot optical depth

Since predicting the ability of pilots to acquire visual contact with the surface or other aircraft is the motivation for precision in ceiling reports, it is appropriate to define cloud base height in terms of cloud optical properties that affect vision. Middleton (1952) describes the factors involved in visual discernment of objects. The first factor is the contrast of an object (e.g., runway markings) against the surrounding background. If L_{vo} is the luminance of an object and L_v' that of the background, then the contrast C is defined as

$$C = \frac{L_{vo} - L_v'}{L_v'} . \tag{8}$$

An ideal black object has C = -1; lights at night can have large positive values of contrast.

The second factor is the alteration of apparent contrast of the object by the optical properties of the atmosphere between the object and the pilot. An important but restrictive special case is horizontal vision when atmospheric optical properties and illumination are homogeneous in the horizontal. These are the conditions for which the familiar Koschmieder relation is valid, and (Middleton, 1952)

$$C_D = C_o \exp(-\sigma D), \tag{9}$$

where C_D is the apparent contrast of the object viewed from a distance D, C_o is the contrast at D = 0, and σ is the extinction coefficient appropriate to the continuum of wavelengths to which the eye is sensitive. The argument of the exponential is the optical depth for the eye, namely $\tau_e = \sigma D$. In the case of a pilot looking downward at a slant angle from near the bottom of a cloud, the analysis is more complicated, and (9) is not strictly valid. Nevertheless, the optical depth τ_e is the yardstick by which the effects of the cloud on the pilot's vision can best be measured. This can be illustrated by examining the two mechanisms by which the apparent contrast is altered (Middleton, 1952). One mechanism is the reduction of the object's apparent luminance by extinction according to

$$L_{vD} = L_{vo} \exp\left[-\int_0^D \sigma(s)ds\right] . \tag{10}$$

Here L_{vo} is the luminance of the object located at D = 0, and L_{vD} is the luminance at the pilot. A similar expression holds for reduction in luminance of the background. The second mechanism is scattering of light into the pilot's line of sight. An expression for this additional luminance L_{vs} that allows for inhomogeneity along the path is

$$L_{vs} = \int_0^D \left[\int_0^{4\pi} L_v(\Theta, s)\, P(\Theta,s)d\omega\right] e^{-\int_s^D \sigma(s')ds'} ds . \tag{11}$$

$L_v(\Theta,s)$ is the luminance as a function of position and scattering angle Θ. $P(\Theta,s)$ is the scattering function, where

$$\int_0^{4\pi} P(\Theta,s)d\omega = \sigma(s) \tag{12}$$

is the scattering coefficient and absorption has been assumed negligible. The integration is over solid angle whose differential is $d\omega$. Note that the exponential term in (11) describes the extinction between the scattering point and the pilot. The importance of the optical depth becomes more obvious if we assume that the amount of light scattered into the line of sight per unit path length is proportional to the extinction coefficient according to

$$\int_0^{4\pi} L_v(\Theta,s)P(\Theta,s)d\omega = L_{vc}\, \sigma(s) , \tag{13}$$

yielding

$$L_{vs} = L_{vc}\left[1 - \exp\left(-\int_0^D \sigma(s)ds\right)\right] . \tag{14}$$

The optical depth

$$\tau_e = \int_0^D \sigma(s)ds \tag{15}$$

is therefore prominent in describing the reduction in apparent contrast due to cloud particles.

The remaining factor in visual discernment is the physiological response of the pilot to the illuminant stimuli. Experiments (Middleton, 1952) have shown that the threshold for contrast detection by humans depends on viewing conditions and the probability level of accuracy that is required. A commonly accepted criterion for practical use is $|C| = 0.05$. As Middleton pointed out, even more conservative criteria are appropriate for aviation safety.

If the luminant source is so small and distant as to appear to be a point rather than an extended source, then Allard's law describes the distance at which the pilot can observe it. Thus

$$ED^2 = I \exp[-\int_0^D \sigma(s)ds] , \tag{16}$$

where E is the illuminance threshold of the eye and I is the source intensity. The optical depth is also prominent in this situation.

A specific definition of cloud base can therefore be formulated by assigning a particular value to pilot optical depth τ_e according to conditions of surface contrast, ambient lighting, and pilot visual ability. The value of τ_e for a pilot at height z_e looking toward the surface at an angle ϕ below the horizontal is

$$\tau_e = \frac{1}{\sin\phi} \int_0^{z_e} \sigma(z')dz', \tag{17}$$

where we assume, as with the RBC, that the extinction coefficient is independent of direction. It should be noted that τ_e is a strong function of ϕ as this angle approaches 0°. An operational definition of ceiling according to the optical depth must therefore incorporate an appropriate choice for ϕ.

3.2 Relationship Between Ceilometer Signals and Pilot Optical Depth

Approximate relationships are derived between optical depth τ_e and the signals from a lidar or RBC. This relationship is used to illustrate how ceilometer signal profiles depend on the pilot optical depth, view angle, and vertical structure of a horizontally homogeneous cloud.

3.2.1 Derivation of fraction of total signal

The pilot's optical depth τ_e can be coupled with the equations for the shape of the lidar and RBC signals with three more approximations. The attenuation coefficients σ_L, σ_R, and σ change with wavelength over the region from 2.75 μm through the visible, which is the wavelength domain of the RBC and anticipated lidar ceilometers. However, when cloud particles are predominantly larger than the wavelength, the change is small because the extinction coefficient is proportional to the geometrical cross-section of the particles. The extinction profile will depend much more on changes in cloud density than the spectral responsivity of the ceilometer. Much of the spectral dependence that may occur can be accounted for by defining the average ratios

$$r_L = \sigma_L/\sigma$$
$$r_R = \sigma_R/\sigma \, . \tag{18}$$

Another approximation valid in the visible and to at least 1.06 μm wavelength in the infrared is that the ratio of extinction to backscatter is approximately the same for a wide variety of cloud size distributions and wavelengths (Derr, 1980; Pinnick et al., 1983). As suggested by Kohl (1978), the lidar backscatter profile can therefore be replaced by

$$\beta_L(z) = \sigma_L(z)/S_L \, , \tag{19}$$

where the extinction to backscatter ratio S_L is approximately constant. For the sake of comparison also assume

$$\beta_R(z,\bar{\theta}_R) = \sigma_R(z)/S_R(\bar{\theta}_R) \quad , \tag{20}$$

where $S_R(\bar{\theta}_R)$ can vary with major changes in scattering angle, but can be considered constant for the signal created by each RBC sweep. The equations for the ceilometer's signal profile can then be written

$$\begin{aligned} b_L(z) &= \frac{r_L}{S_L}\,\sigma(z)\,\exp[-g_L \int_0^z \sigma(z')dz'] \\ b_R(z) &= \frac{r_R}{S_R}\,\sigma(z)\,\exp[-g_R \int_0^z \sigma(z')dz'] \quad , \end{aligned} \tag{21}$$

where

$$\begin{aligned} g_L &= 2r_L/\sin\theta_L \\ g_R &= r_R\left(1 + \frac{1}{\sin\bar{\theta}_R}\right) . \end{aligned} \tag{22}$$

Our definition for cloud base is the height z_e at which the optical depth along the pilot's line of sight equals τ_e as given in (17). In order to obtain z_e from the ceilometer signal we integrate the profile shape equation b_L in z to obtain

$$B_L(z_e) = \int_0^{z_e} b_L(z')dz' \quad . \tag{23}$$

This is accomplished analytically through the change of variables

$$\begin{aligned} T &= \exp[-g_L \int_0^z \sigma(z')dz'] \\ dT/T &= -g_L\,\sigma(z)dz \quad , \end{aligned} \tag{24}$$

where T is the vertical transmission. Thus (23) becomes

$$B_L(z_e) = \frac{r_L}{S_L g_L}\,[1 - T(z_e)] \tag{25}$$

or

$$B_L(z_e) = \frac{r_L}{S_R g_R} [1 - \exp(-g_L \sin\phi \ \tau_e)] \ . \qquad (26)$$

The RBC's expression is

$$B_R(z_e) = \frac{r_R}{S_R g_R} [1 - \exp(-g_R \sin\phi \ \tau_e)] \ . \qquad (27)$$

As a simple example of how (26) might be used, assume that the lidar points vertically so $\sin\theta_L = 1$. Assume also that S_L, r_L, and the calibration factors K_L and F_L in (2) are also known. A choice of ϕ and τ_e define the pilot altitude z_e, which must be found from the lidar profile. Then

$$\int_0^{z_e} \frac{P_L(z')}{F_L(z')} dz' = \frac{K_L r_L}{S_L g_L} [1 - \exp(-g_L \sin\phi \ \tau_e)] \qquad (28)$$

relates the lidar signal to the cloud base height z_e. Since all the factors on the right hand side are determined, z_e is found by integrating the range-corrected lidar signal from $z = 0$. In practice, the lidar and cloud optical factors are not known exactly, the lidar signal will be contaminated by noise to some degree, and the real-world values of ϕ and τ_e will vary from case to case. The interpretation of the lidar signal thus can provide only an estimate of the height where a pilot will attain visual contact. This formulation is particularly weak for practical use because of the uncertainties associated with S_L and K_L.

With one additional assumption, which is satisfied most of the time, the need for explicit knowledge of K_L and S_L is eliminated. As recognized by Platt (1973) and Kohl (1977), if the cloud is optically dense such that the round-trip transmission of the ceilometer radiation approaches zero before the measurement reaches cloud top, then the total cloud signal is

$$\begin{aligned} B_L^T &\simeq r_L / S_L g_L \\ &= B_L \ (z \to \infty) \ . \end{aligned} \qquad (29)$$

In practice the cloud need not extend vertically without limit; it is only necessary that the return from near cloud top be strongly attenuated. The fraction of total signal (FOTS) is defined as

$$\text{FOTS} \equiv \frac{B_L(z_e)}{B_L^T} = 1 - \exp(-g_L \sin\phi\ \tau_e) \ . \tag{30}$$

The FOTS expression for the RBC is identical except that g_R replaces g_L.

FOTS provides an objective relationship between the ceilometer signal and the defined optical depth between the pilot and the surface. The lidar calibrates itself for the optical depth measurement by assuming that the attenuation at large range is so great as to drive the round-trip transmission to zero, and by assuming the extinction to backscatter ratio is constant. Figure 3 illustrates how the numerical operations are performed. The geometrical factors (and any minor wavelength dependence) determine g_L, and the parameters ϕ and τ_e describe the point at which the pilot is considered to be at cloud base. Two integrations are then performed on the range-corrected signal. The first is over the complete profile to establish the calibration. The second is from $z = 0$ until the FOTS value is reached, which yields z_e. Aside from any promise the FOTS method may have as an operational signal-processing technique for a ceilometer, it is used in this paper as an analytical tool to evaluate the relationships between ceilometer signal profiles and the optical depth encountered by a pilot.

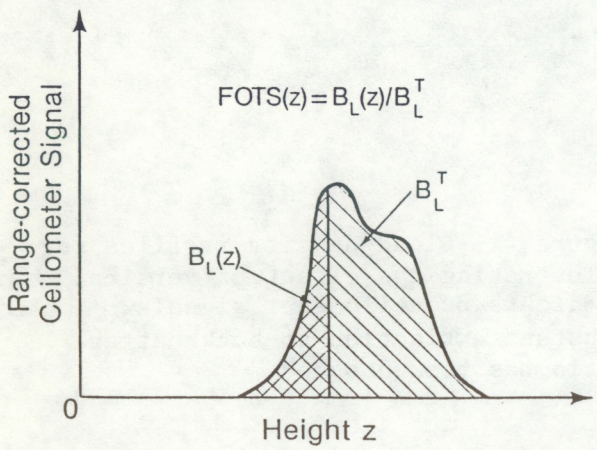

Figure 3.--Signal integrations in FOTS method. B_L^T is the total area, and FOTS is the fraction up to height z.

3.2.2 Examples with FOTS method

Some examples of cloud profiles, the associated ceilometer signal profiles, and FOTS values are next considered using a few simple cloud models. The vertical profiles of cloud density (Fig.4) were designed to show some general characteristics of ceilometer signals and do not purport to exactly duplicate any cloud profiles commonly found in nature. The abscissa is the height z* from the lower fringe of the cloud as normalized by the characteristic extinction coefficient σ_o. For instance, if the homogeneous cloud has $\sigma_o = 10\ km^{-1}$, then the graph shows the cloud for $0 \leq z^* \leq 0.4$ km. The ordinate shows the relative magnitude of backscatter coefficient. The three profiles with gradual increases all have the same slope at $z^* = 0$. Figure 5 gives the $b_L(z)$ profile in relative units for a vertically-pointing lidar, assuming constant S_L. The normalizing factor b_o is the range-corrected lidar signal from the bottom fringe of a homogeneous cloud of density β_o. The peak signal is at the lower boundary for the homogeneous profile, but is smoother and displaced upward in the clouds with gradual vertical increases in cloud density. The nearly identical positions of the peaks in b_L for the three gradually increasing distributions is somewhat fortuitously caused by the competing factors of increasing local density versus greater attenuation up to peak. These gradually increasing distributions are not radically different up to the peak, where attenuation becomes large and b_L starts to diminish. Above the peak, however, the b_L profiles rapidly diverge.

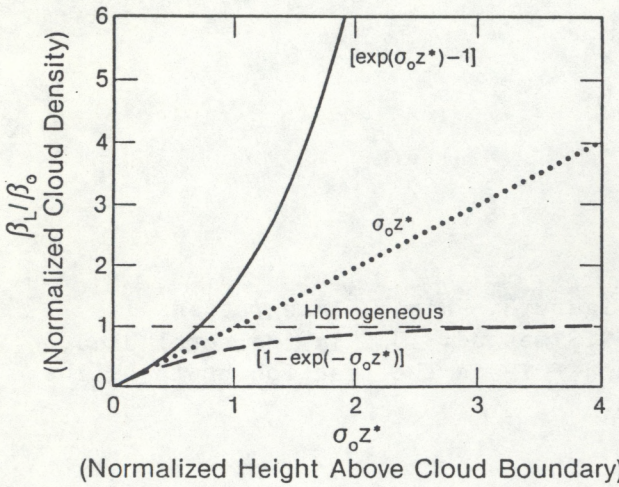

Figure 4.--Cloud density profiles for illustrating the effect of vertical gradients on ceilometer signals. Constant extinction-to-backscatter ratio has been assumed.

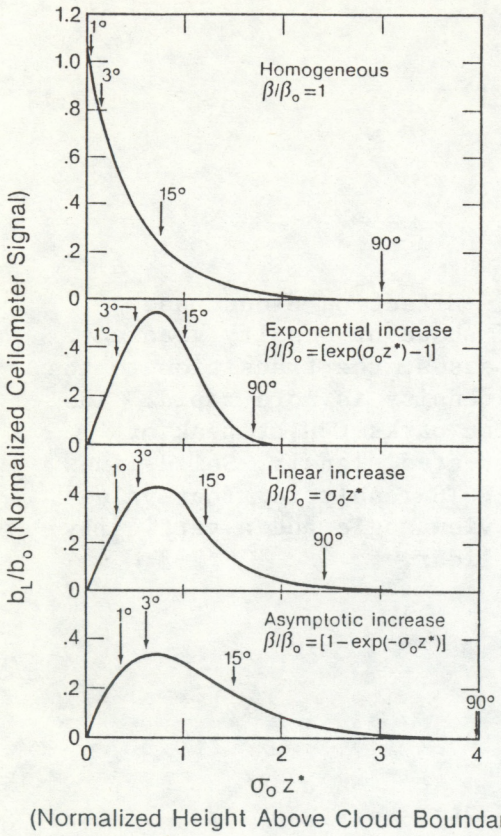

Figure 5.--Range-corrected ceilometer signals for the cloud density profiles of Fig. 4. The lidar points vertically. The arrows show pilot altitude where $\tau_e = 3.0$ with pilot view angle ϕ as indicated.

In order to show some examples of pilot altitudes for visual contact, we have selected an optical depth $\tau_e = 3.0$, corresponding to contrast transmission of .05, and four viewing angles ϕ: 90°, 15°, 3°, and 1°. These angles respectively correspond to the pilot looking straight down, at a nominal cockpit cut-off angle, along the flight path during an instrument approach and at the surface at a large distance. The corresponding FOTS values, assuming $r_L = 1$, are .99752, .7884, .2695, and .0994. The arrows in Fig. 5 indicate the pilot's altitude upon attaining the cloud base height by the FOTS definition. For the homogeneous cloud the FOTS values all occur at elevations higher than the peak in b_L. For the three gradual profiles the peak occurs at FOTS values corresponding to $\tau_e = 3.0$ and $\phi \approx 5°$. The FOTS points for the nadir-viewing pilot vary considerably in z*.

Figure 6 demonstrates the effect of the rate of approach of cloud density in the vertical to a homogeneous value. The cloud density profile is

$$\frac{\beta}{\beta_o} = 1 - \exp(-a\ \sigma_o z^*) \ . \qquad (31)$$

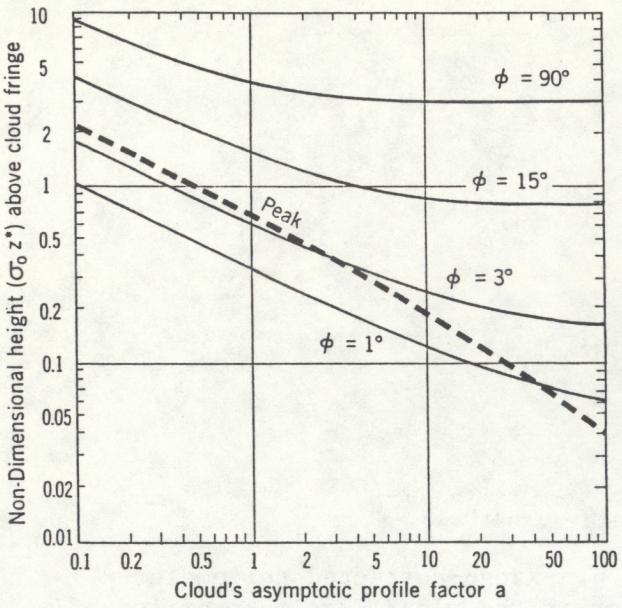

Figure 6.--Effect on cloud base height of shape of density gradient. As a increases, the transition to the interior density is more rapid. The dashed line marks CBH at peak of range-corrected signal. Solid lines show the FOTS result for four values of pilot view angle and a vertically-pointing lidar.

The range-corrected lidar signal profile is

$$\frac{b_L}{b_o} = [1 - \exp(-a\ \sigma_o z^*)]\ \exp(-2\sigma_o z^*)\ \exp[-2(1 - e^{-a\ \sigma_o z^*})/a] \quad . \quad (32)$$

The ceilometer signal in Fig. 5d is for a = 1. As $a \to \infty$, the homogeneous distribution in Fig. 5a is approached, while for small a the cloud density increases very slowly. Figure 6 plots the nondimensional height for the four selected values of FOTS as a function of the parameter a. Note that the position of the peak ceilometer signal is higher than the FOTS point for $\phi = 1°$ and 3°, except when a is large (homogeneity approached rapidly). This demonstrates that the position of the peak ceilometer signal is a conservative choice for cloud base when the cloud has a sharp transition from clear air to interior density. The position of peak signal from a vertically pointing lidar for clouds with a gradual increase in density is adequate for $\phi = 3°$ and $\tau_e = 3.0$, but may be too high if smaller τ_e or ϕ is appropriate.

Figure 7 displays the dependence of FOTS on the ceilometer pointing direction. The abscissa is the average RBC angle or the elevation angle of a lidar ceilometer. The ordinate is the FOTS value. The curves are for discrete values of combined pilot optical depth and view angle. r_L and r_R have been assumed equal to unity. As the lidar elevation angle decreases

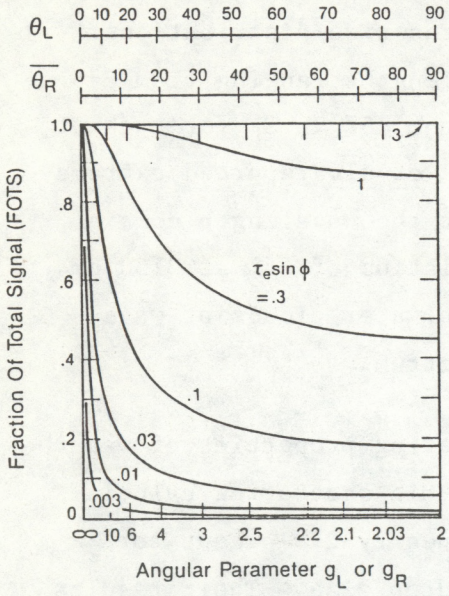

Figure 7.--Dependence of FOTS value on ceilometer pointing angle.

from 90° the FOTS value increases for any constant $\tau_e \sin\phi$. For the RBC the FOTS value increases with decreasing cloud height and $\bar{\theta}_R$. It must be kept in mind that Fig. 7 plots the idealized FOTS equations with no allowance for possible departure from the assumptions applied during their development.

3.3 Effect of Nonideal Factors on Ceilometer Signals

3.3.1 Nonuniform extinction to backscatter ratio

The FOTS method includes the critical assumption of constant extinction to backscatter ratio S_L for the obscuration. Circumstances where S_L can be considered constant with high reliability will first be documented. Conditions where the assumption is problematic will then be covered, including an analysis of errors.

The simplest realization of constant S_L occurs when the particles do not vary in optical properties (i.e., size distribution, shape, and composition) in the region of interest at the bottom of the cloud, although variation in number density is permitted. Unfortunately, it is unreasonable to expect the size distribution always to be constant in the transition zone from clear to cloudy air (e.g., Noonkester, 1984). However, during periods of poor visibility near the surface due to fog or precipitation, the size distribution may often be uniform.

Derr (1980) and Pinnick et al. (1983) have shown that S_L is approximately the same for a wide variety of typical liquid cloud drop size distributions. They reached this conclusion for each of several wavelengths ranging from 275 to 1064 nm. Derr reported a standard deviation of about 15% in S_L for each of the seven wavelengths in his calculations, and Pinnick et al. reported extreme differences of 50% at 1064 nm. Derr demonstrated that the wavelength domain of constant S_L is limited by obtaining a standard deviation of 64% at 3750 nm. The approximation of constant S_L is therefore valid in water clouds at wavelengths within or near the visible portion of the spectrum.

Shipley and Weinman (1978) investigated the scattering properties of water spheres possessing sizes typical of raindrops. Their Mie scattering calculations showed that the extinction efficiency was very nearly 2.0 except for slight variations with fine changes in wavelength or drop size. Their results for backscatter efficiency, averaged over a narrow band of drop sizes, do vary somewhat with the size parameter. Using $S_L = 4\pi/P(180°)$, where $P(\theta)$ is the normalized scatter phase function, and assuming 1064 nm wavelength, one calculates from their results an S_L equal to 17.5 sr for 34 μm drop radius, decreasing gradually to 13.3 sr for 144 μm radius, and then increasing again to 19.8 sr at 765 μm radius. For a spectrum of drop sizes the average S_L can be expected to lie somewhere between the two extreme values. The raindrop values are close to the $S_L = 18$ sr found by Derr and Pinnick et al. for clouds. The assumption of constant S_L is therefore reasonable for liquid precipitation, both below and within clouds.

Characterization of S_L for ice particles is more difficult, because Mie scattering does not apply to the irregular crystalline shapes they usually possess. The available information indicates that S_L is usually larger for ice than for spherical water drops, and possibly more variable. Platt (1981) summarized lidar measurements for cirrus by several researchers, who obtained $26 \lesssim S_L \lesssim 84$ sr. Platt and Dilley (1984, Table I) report more recent measurements of $23 \lesssim S_L \lesssim 63$ sr, including a systematic variation with temperature. From their Figures 4 and 5 one obtains $14.5 \lesssim S_L \lesssim 36$ sr. Platt et al. (1978) showed that backscatter for a lidar pointed precisely at the vertical can be strongly enhanced by specular reflection from oriented plate crystals, which would result in unusually small values of S_L. The ray optics calculations of Wendling et al. (1979) for hexagonal plates and columns produced

$10 \lesssim S_L \lesssim 50$ sr. The laboratory studies of Sassen and Liou (1979) at warmer temperatures than is common for cirrus produced S_L values for artificial ice clouds that were typically five times larger than for water clouds in the same equipment. All these results are restricted to the visible portion of the spectrum. The author is not aware of any studies of S_L in snow. These data on ice particles warn that the assumption of constant S_L in the presence of frozen or mixed-phase clouds or precipitation is subject to question.

Errors will occur in predicting the height z_e by the FOTS method if S_L is not constant. The severity of the error will depend on the location as well as the magnitude of the variations in S_L. A simple analytical profile assumed for S_L will provide some idea of the nature and magnitude of these errors. With transmission T for the ceilometer defined by (24), denote S_L at the bottom fringe of the cloud where T = 1 as S_{Lo}. Let S_L at T = 0 deep within the cloud be $S_{L\infty}$. Letting S_L vary linearly with the transmission gives

$$S_L(T) = S_{L\infty} + (S_{Lo} - S_{L\infty})T \ . \tag{33}$$

From (24) it can be seen that T and, hence S_L are most sensitive to changes in optical depth at the fringe rather than deep within the cloud. The correct FOTS value for this model of nonuniform S_L is

$$\text{FOTS} = 1 - \frac{\ell n[1 + (S_{LO}/S_{L\infty} - 1)T(z_e)]}{\ell n[S_{LO}/S_{L\infty}]} \tag{34}$$

Figure 8 gives the pilot optical depth that occurs as a result of erroneously assuming S_L is constant. τ_e (assumed) is the optical depth that the ceilometer is asked to predict. τ_e (actual) is the true optical depth for the pilot at the height z_e produced by the FOTS method when S_L is incorrectly assumed constant. If S_L decreases (increases) with height, the predicted τ_e and also z_e are too high (low). The error is worse for small values of FOTS because the pilot views only through a region where $S_L \approx S_{Lo}$, whereas the whole range of $S_L(T)$ influences the predicted height. If $S_L(T)$ fluctuates about some mean value, the error in z_e is likely to be less because of the integrating nature of the FOTS method. Large monotonic gradients in S_L of

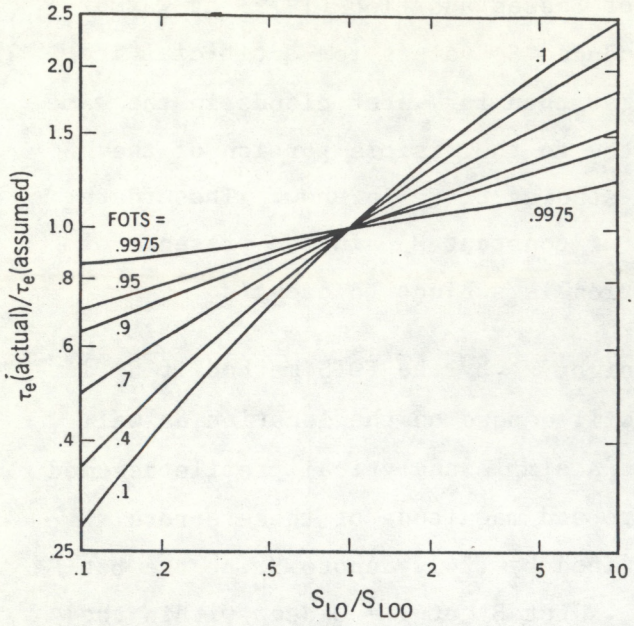

Figure 8.--Example of bias in optical depth when extinction to backscatter ratio is not uniform.

a factor of 2 or more can produce substantial errors in τ_e. If S_L changes by less than 30% the errors in τ_e are no more than 25%.

3.3.2 FOTS for thin clouds

The FOTS method assumes that the cloud along the optical path of the ceilometer is so dense that extinction reduces the signal from far within the cloud to effectively zero. Optically thin clouds introduce a biased error into the estimate of pilot altitude for visual contact because the denominator of (30) is smaller than for thick clouds. If the FOTS value appropriate to a thick cloud is used, then the resulting value $z_e(\text{thin})$ is different from z_e, and the optical depth $\tau_e(\text{thin})$ along the pilot's line of sight from $z_e(\text{thin})$ also differs from τ_e. The amount of bias for a lidar ceilometer is given by

$$\frac{\tau_e(\text{thin})}{\tau_e} = \frac{\ell n[1 - (1 - e^{g_L \tau_c})\text{FOTS}]}{\ell n[1 - \text{FOTS}]} , \tag{35}$$

where

$$\tau_c = \int_0^\infty \sigma(z)dz \tag{36}$$

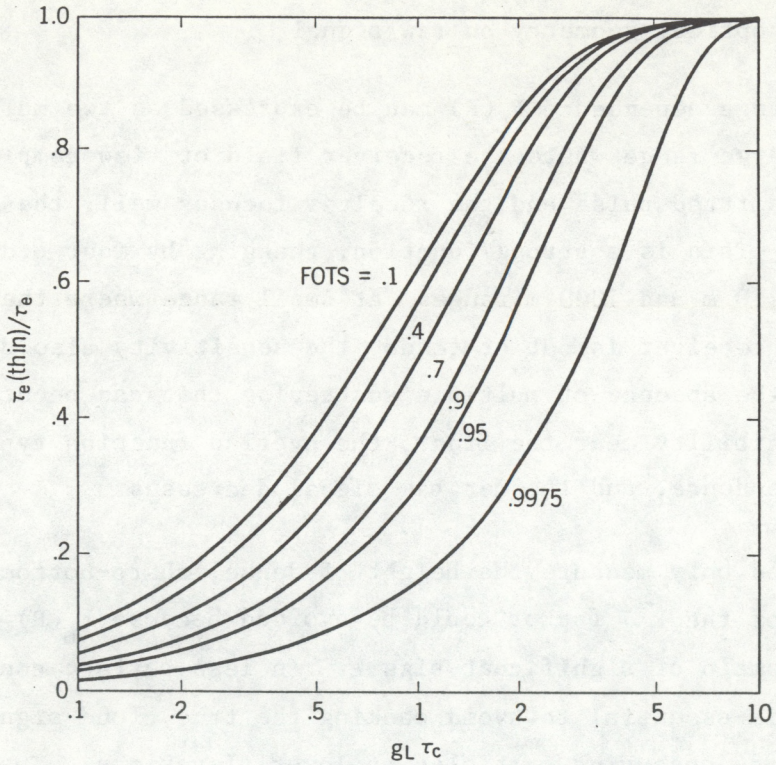

Figure 9.--Bias in predicted optical depth when a cloud is not optically thick. τ_c is the vertical optical depth of the cloud.

is the one-way optical depth vertically through the cloud. For the RBC, g_R replaces g_L. Figure 9 plots (35) for several values of FOTS. Since the ratio does not exceed unity, the error is conservative; i.e., the FOTS method estimates a lower altitude for visual contact when the cloud is thin.

In order to illustrate that the ratio in (35) rarely deviates far from unity, assume a cloud, viewed vertically, through which blue sky can still be perceived; estimate roughly that $\tau_c = 2$. Consider a vertically-pointing lidar, $\tau_e = 3.0$, and $\phi = 15°$. The ratio from (35) is then .9575, which is a trivial deviation for practical purposes. For very thin layers ($\tau_c \lesssim 1$) the ratio deviates substantially from unity. In such cases, however, the use of the FOTS technique seems just as efficacious as height for peak signal in characterizing the presence and position of the cloud.

As the optical density of a layer becomes extremely thin ($\tau_c \ll 1$), some procedure is desirable in any ceilometer for choosing a report of no cloud in order to avoid false alarms. For a peak detector, the range-corrected signal might be required to exceed a certain threshold. In the FOTS method, a threshold might be applied to the integral of the range-corrected signal.

3.3.3 Effects of optical geometry on raw signal

The lidar's range dependence $F_L(R)$ can be expressed as two multiplicative components. At large range where the receiver field of view completely overlaps the transmitted pulse and the receiver focuses well, the sensitivity decreases as R^{-2}. This is a strong function, changing by four orders of magnitude between 10 m and 1000 m range. At small range where the overlap is incomplete or the receiver is out of focus, the sensitivity also diminishes. As $R \to 0$, and in the absence of multiple scattering that can occur during conditions of low visibility near the lidar, the overlap function typically dominates the R^{-2} dependence, and the net raw signal decreases.

If a lidar need only measure the height of dense, sharp-bottomed clouds, then correction for the R^{-2} factor could be avoided because $F_L(R)$ would change little over the domain of significant signal. In less perfect conditions a range correction is essential to avoid masking the true cloud signal by strong raw signal from less obscuring particles at lower elevations. The signal $P_L(R)$ from moderate precipitation, dense haze, or blowing dust could easily exceed the raw signal from higher clouds. One straightforward method to avoid this error is to digitize the raw signal and compute the correction. Analog compensation in the detector or receiver electronics might also prove efficacious. The diminishing factor in the near field is very sensitive to the optical design and alignment and is considerably more complex than the R^{-2} dependence.

The range sensitivity of the RBC has not been studied as carefully as the lidar's, presumably because the RBC has a narrower application and greater degree of complexity. Experience has shown that RBC signals from high clouds are generally weaker than from low clouds. Early models of the RBC were fitted with operator controls to adjust sensitivity, while later models possess automatic gain control circuits. These controls adjust the overall gain, effective for the entire sweep, but do not compensate for $F_R(\theta_R)$ during the sweep. The analysis in the Appendix shows that F_R is approximately independent of θ_R if the optical thickness is not large across the volume of intersection of the transmitter and receiver, and if $\theta_R \lesssim 85°$. The RBC shows

no deterioration in sensitivity as the scatterers lower to $\theta_R \to 0°$. Within these limits the raw signal $S_R(\theta_R)$ can substitute for b_R without range correction. This is no longer true when the optical depth of the beam path between entry and departure of the intersecting volume becomes significant. In this case F_R decreases as θ_R increases. In the limit as $\theta_R \to 90°$, the detector output depends on H^{-2}. However, the mild θ_R dependence of the RBC's sensitivity over a large portion of its operating range has enabled its effective use even in the absence of electronic conditioning of the signal.

Unlike the lidar, where the scattering angle is always the same, the scattering coefficient $\beta(\theta_R)$ will vary somewhat as θ_R changes between 0° and 90° (or scattering angle changes between 90° and 180°). This can be interpreted as a change in system sensitivity. For most cloud size distributions $\beta(\theta_R)$ increases gradually as θ_R increases, with peaks at the rainbow angle and near backscatter (e.g., Deirmendjian, 1969). This increase in $\beta(\theta_R)$ partly compensates for declining RBC sensitivity at high RBC angles.

Overall, the RBC's raw signal depends much less on cloud height than the lidar's signal.

3.3.4 Finite spatial resolution

Compared with profiles from a theoretically ideal instrument, profiles from a lidar or RBC are smeared. The finite volume occupied by the probing radiation and the limited electronic response time of the receiver cause this smearing.

The pulse length and response time of the WPL lidar produced a signal from a single target corresponding to range resolution of approximately 7 m full width at half maximum. The signal was mildly asymmetric with a faster rise than fall. A lidar ceilometer might endure coarser resolution in trade for lower engineering costs. The divergence angle of a lidar ceilometer would probably be very narrow, giving better transverse than longitudinal resolution. It should be noted that a narrow divergence angle is also an asset in achieving good signal-to-noise ratio and limiting the effects of multiple scattering. On the other hand, a wider angle can smooth out sharp signal fluctuations that are caused by small-scale variation in cloud density or pre-

cipitation. Eye safety may also require a wider divergence angle. Various design considerations therefore influence the choice of lidar divergence angle.

The angular dimensions of the RBC's beam and the receiver's field of view in the vertical plane (ψ_{tp} and ψ_{rp} in Fig. A1) affect the finite resolution of the RBC as the pulse length affects the lidar's range resolution. The RBC signal width can be easily illustrated by assuming that the transmitted beam is uniform in intensity with $\psi_{tp} = 1.0°$ width. Similarly, the receiver field is considered uniform with $\psi_{rp} = 0.9°$. An examination of the RBC geometry shows that the overall width of the RBC response is given by

$$\psi = \psi_{tp} + \psi_{rp} \sin^2 \theta_R \, . \tag{37}$$

For $\theta_R \simeq 0°$, only the transmitted beam width is important, whereas at $\theta_R \simeq 90°$ the spread in the receiver field of view attains its greatest additional effect. The total response time of the RBC signal, including electronic spread, was measured by holding a short board above the receiver to create a point target. The signal pulse, after demodulation and amplification but before recording, was 1.5° full width at half maximum and 2.7° entire width. This was considerably larger than the expected 1.0° entire width, indicating substantial spreading due to receiver electronic response or inaccuracy in the calculation of the beamwidth. The shape of this test signal was almost symmetrical.

A ceilometer's finite resolution affects the shape of the ceilometer signal in several respects as illustrated by the RBC. The most obvious effect is that sharp features are smeared, which can introduce uncertainty into the designation of the location of peak signal or other criteria for interpretation. This problem is particularly troublesome at large RBC angles, where the instrument response alone can be wider than the signal a cloud would otherwise produce. The location of identifying features can also shift. Figure 10 provides an example of the ideal RBC signal from a homogeneous cloud before and after the instrumental broadening. The example assumes uniform optical sensitivity within ψ_{tp} and ψ_{rp}, RBC baseline of 244 m (800 ft), cloud fringe likewise at 244 m or $\theta_R = 45°$, and $\sigma = 20$ km^{-1} inside the cloud. The finite-

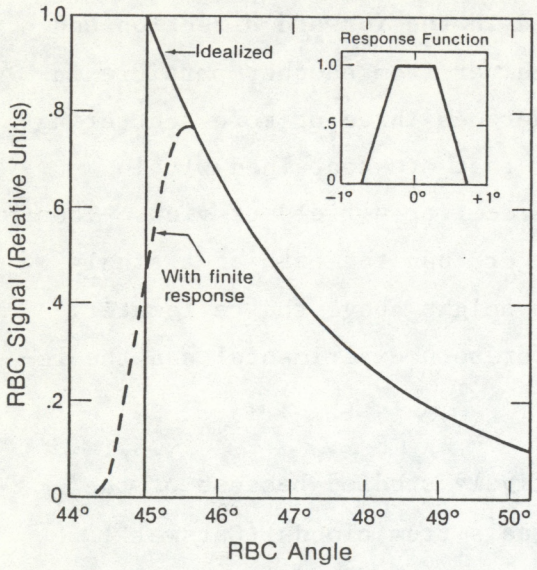

Figure 10.--Smearing and shift of peak signal due to theoretical RBC finite resolution. The finite response is the convolution of the response function with the idealized response.

response curve peaks 0.58° or 5.0 m higher than the peak in the idealized signal. If the cloud fringe is raised to 1384 m where θ_R = 80°, the idealized signal is much narrower and the smearing more pronounced. The finite response then shifts the peak 0.12° or 17 m higher. With cloud fringe at 65 m or θ_R = 15° the shift is 0.50° or only 2.3 m. Since the measured single-target signal from the RBC was wider than calculated from ψ_{tp} = 1.0°, the actual amount of smearing and shift is expected to be greater than calculated in these examples.

If a ceilometer's spatial resolution is finer than the required reporting accuracy, it is reasonable to assume that spreading effects can be ignored. If the spatial resolution is larger, performance may still be adequate, but the effects of smearing and shifting should be evaluated.

3.3.5 Multiple scattering

Single scattering has been assumed thus far, which means that every transmitted photon that reaches the detector has traveled an uninterrupted path through the air except for one scattering event. The scattering particle must necessarily be in the path of the transmitted radiation as well as the receiver's field of view. All other photons are considered lost from the system. In dense scattering media such as clouds, a substantial fraction of the photons reaching the receiver may undergo more than one scattering event.

For instance, a photon might first be scattered in the forward direction and then be scattered a second time toward the receiver from another particle in the receiver's field of view. If a photon undergoes three or more scattering events, some of these could occur in locations that are contained within neither the original transmitter beam nor the receiver's field of view. The path of a multiply scattered photon can be longer than the path of a singly scattered photon that reaches the same maximum height above the ceilometer. Multiple scattering is a challenging problem for both experimental and theoretical approaches.

Multiple scattering for lidar has been actively studied because of the interest in quantitative interpretation of signals from clouds (Carswell, 1981) and other dense media. Theoretical treatments have been successful in revealing the important characteristics of multiple scattering. The cloud's optical properties and the optical geometry of the lidar both determine the amount of multiple scattering. The main factors are (Zuev, 1982) the optical density of the cloud as given by the scattering coefficient and the diameter of the receiver's field of view in the cloud. The amount of multiple scattering increases with these factors. The degree of multiple scattering also depends on the asymmetry in the scattering phase function. A size distribution with large drops, which has a strong, narrow peak in the forward direction of the phase function, causes more multiple scattering in the lidar signal than a size distribution with identical scattering coefficient but more isotropic phase function (Weinman, 1976). Lidar design can reduce the amount of multiple scattering by shrinking the divergence angle of the receiver's field of view.

Multiple scattering can alter the signal profile of a lidar ceilometer. Multiple scattering produces a larger signal in the receiver than single scattering. The relative importance of multiple scattering increases from a negligible amount at the bottom fringe of a cloud until it dominates the return from large optical depth within the cloud. Figure 11 is based on two calculated examples from Plass and Kattawar (1971) of the range-corrected signal for all orders of scattering compared with single scatter. For the homogeneous cloud, the multiply scattered signal decays in approximately exponential fashion but at a slower rate than the single-scatter component.

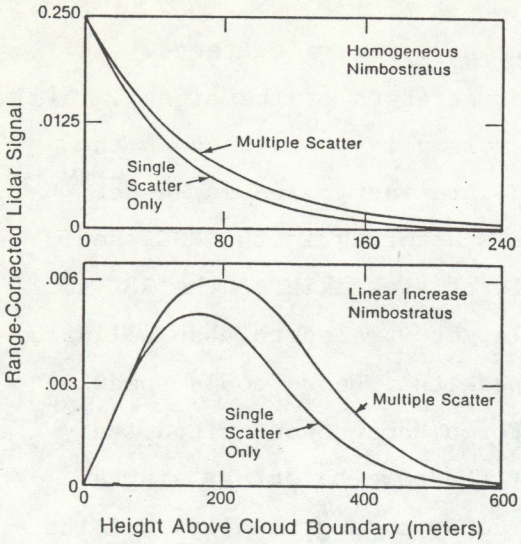

Figure 11.--Multiple scattering in model clouds. The degree of multiple scatter increases with optical depth. (From Plass and Kattawar, 1971.)

Multiple scattering enhances the tail of the ceilometer signal from deep within the cloud more than the leading part from the cloud fringe. For the other cloud in Fig. 11, where density increases linearly with height, the stronger enhancement from the deeper part of the cloud leads to an upward shift of the position of the peak. This shift could be compounded if the lidar also had poor spatial resolution. If the location of peak signal is used as the criteria for cloud base, multiple scattering will bias the result to a greater height.

The author is unaware of any investigation of multiple scattering that applies to the geometry of the RBC. However, similarities exist between the two types of systems. The transmitters in both types project radiation in a collimated beam of narrow dimensions, but the lidar's can be considerably narrower. Each receiver also has a field of view with narrow angular dimensions, but again the lidar's typically is smaller. The RBC operates in the near IR where the phase function for most clouds will have a strong peak in the forward direction, but usually not as sharp as in the visible. The lidar relies on backscatter to divert the path of the radiation from the transmitter toward the receiver, while the RBC functions at scattering angles between 90° and 180°, depending on θ_R. One other difference is that multiple scattering in the lidar can slightly increase the time of flight of a photon compared with a singly scattered photon reaching the same maximum range, whereas time of flight is of no consequence in the RBC. The general features of multiple scattering in the RBC can be extrapolated from the results for lidar.

Multiple scattering in the RBC is expected to have several effects. As with lidar, multiple scattering will increase the strength of the signal. This enhancement will be minor when the intersecting volume is restricted to the bottom fringe of the cloud, but will grow as the intersection moves deeper into the cloud. The ratio of multiple to single scattering in the RBC should be comparable with that of a lidar having a field of view akin to the RBC's 1-4° angular dimensions. The RBC might have a larger wavelength than a lidar, which could lead to a wider forward-scattering peak that hence could somewhat moderate the multiply scattered contribution. For a homogeneous cloud the RBC's multiply scattered return should peak near the same height as single scatter (spatial resolution effects aside), but decay more gradually. If the cloud density increases with height, the peak should shift upward. Multiple scattering in the RBC can create additional signal corresponding to lower heights because, unlike the lidar, time-of-flight is not a consideration. This can occur when the beam intercepts the cloud beyond the receiver field of view, and light is scattered back to the field of view and then again toward the receiver. As the RBC angle nears 90° the multiple scattering approaches behavior that is symmetric about the nominal angle at peak signal. Overall, multiple scattering is expected to be more dominant in the RBC signal than in the lidar signal because the divergence angles of the RBC transmitter and receiver are larger than those of a practical lidar ceilometer.

3.4 Slant Visual Range

The FOTS method can determine the slant visual range when the assumptions in its derivation are adequately met. Its prospects for augmenting or replacing other signal analysis techniques are worth noting. The concept for measurement of slant visual range usually involves a lidar pointing at a low angle up the aircraft approach path. The well-known slope and ratio methods are two related approaches that can produce good results when the obscuration along the lidar path is relatively uniform, but Kohl (1978) and Gaumet and Petitpa (1982) are among those who have emphasized how these methods can fail when conditions depart from homogeneity. Gaumet and Petitpa illustrate how a scanning lidar can detect the existence of such inhomogeneties, but the slope and ratio methods are then unable to predict the slant visual range. Gaumet and Petitpa also reiterate the problems of the signal's large dynamic range and multiple scattering that arise in this concept.

The FOTS method can overcome the limitations of nonuniform obscuration. Since FOTS requires only a uniform extinction to backscatter ratio, it might usually be successful even when the obscuration itself is not uniform. A scheme that checks for very large optical depth along the beam should be included, if possible, before invoking FOTS. A system for measuring slant visual range should be able to select either the slope or the FOTS method as appropriate.

The elevation angle of the lidar influences the extent of the signal's dynamic range and the degree of multiple scattering. If the lidar is aligned parallel to the pilot's view the round-trip attenuation is $\exp(-2\tau_e)$, which is .0025 for $\tau_e = 3.0$. This dynamic range is multiplied by the R^{-2} decrease in received signal strength. Although a measurement coincident with the pilot's line of sight is obviously desirable, the resulting hardware specifications are demanding. If the sensor aims at a higher angle θ_L the attenuation to the pilot height z_e is reduced to $\exp(-2\tau_e \sin\phi/\sin\theta_L)$. The degree of multiple scattering also increases in an accelerating fashion with the depth of penetration. The amount of multiple scattering between the surface and z_e becomes less severe at higher lidar elevation angles. The optimum device for measuring slant visual range might therefore operate at a higher elevation angle than the pilot's view, trading exact spatial coincidence for less demanding hardware specifications and simpler corrections for multiple scattering.

4. EFFECTS OF HORIZONTALLY INHOMOGENEOUS CLOUDS

Clouds frequently display a variation in the height of the bottom in time and space. Khrgian (1963) summarized the reports of several researchers regarding the variability of height to cloud bottom of stratiform clouds. These variations are commonly observable by eye from the surface as texture in the appearance of cloud bottom. From an aircraft flying near cloud bottom the variation exhibits itself as obvious changes in cloud density. The undulations may exhibit a rather periodic structure, or at other times they may be uneven and chaotic in appearance. Episodes of variable cloud bottom were common during the course of WPL's ceilometer comparison. Davis (1969) performed statistical analysis on CBH variations measured by a British cloud-base recorder and found during four low-cloud events totaling 6 hours that

$$\rho = 4h^{1/2}\, t^{1/6} \quad , \tag{38}$$

where ρ is the standard deviation of differences in CBH at times t minutes apart, and h is the mean height of cloud base in feet. Such horizontal variability violates the simple assumption of a homogeneous cloud upon which ceilometry seems to be based. The effect of this variability on ceilometer signals and pilot visibility should be considered.

The primary effect on a typical ceilometer's output will be a temporal variation of CBH. The pilot at cloud bottom will experience some intermittency in holding contact with the visual cues at the surface. Since a pilot usually views along a shallow angle while the ceilometer might probe more vertically, it is not clear how the statistics of the ceilometer reading can be used to predict the pilot's visual experience. For instance, if the lowest protrusions are optically dense, the pilot might be able to sustain visual contact only when considerably below the average CBH from the ceilometer.

To examine such circumstances in a quantitative manner, a simple cloud model with undulating bottom can be used. The model is intended only to reveal some general characteristics of ceilometer and pilot performance and should not be considered a complete or exact description of cloud base undulations. The model sinusoidally varies the height of the cloud's bottom fringe but is otherwise uniform in its density and optical properties. Mathematically the scattering coefficient is expressed as

$$\sigma = \begin{cases} 0 & z^* < \frac{\Delta z}{2}\,[1 + \cos(2\pi\, x/\Delta x)] \\ \sigma_o & \text{otherwise} \end{cases} \quad , \tag{39}$$

where Δz is the peak-to-peak variation in height of cloud fringe, and Δx is the horizontal distance between neighboring cycles. The cloud is assumed optically dense in the vertical and hence mathematically extends to infinity for the current purpose.

Figure 12 shows the visual contact maintenance height (VCMH), which is defined as the height at which a pilot can sustain visual contact with the

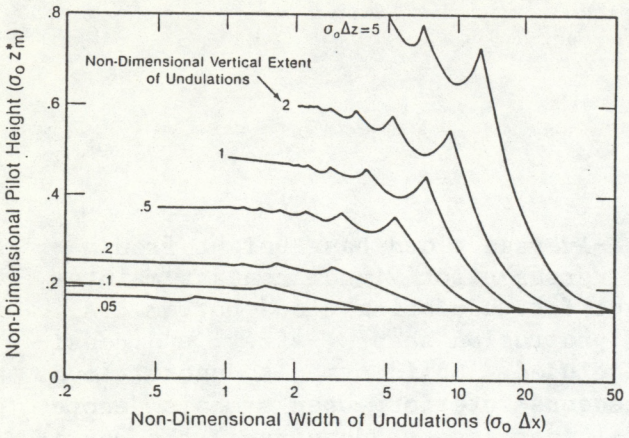

Figure 12.--Pilot's visual contact maintenance height for undulating cloud bottom. The cloud interior is homogeneous in density. View parameters $\tau_e = 3.0$ and $\phi = 3°$ were assumed.

ground no matter what his horizontal position. The calculation assumed $\phi = 3°$ and a threshold optical depth for the pilot of $\tau_e = 3.0$. The optical depth at this view angle varies somewhat according to the pilot's position relative to the protrusion. The VCMH was the smallest height at which the pilot's optical depth did not exceed 3.0. The figure plots the results in optical depth rather than spatial coordinates. The ordinate gives VCMH, the abscissa gives the horizontal size of the undulations, and the curves are for a series of protrusion vertical sizes $\sigma_o \Delta z$.

One interesting characteristic is the collapse of all curves to $\sigma_o z^*_m = .157$ (the flat cloud value) when $\sigma_o \Delta x$ is large. This occurs when a single, very broad protrusion limits the pilot's view, and the VCMH is the same as if the cloud were flat with bottom positioned at the level of the lowest protrusion. Another characteristic is the approach of VCMH to a constant value, dependent on $\sigma_o \Delta z$, when $\sigma_o \Delta x$ becomes small. This situation occurs when a pilot's vision can penetrate many protrusions, encountering limited optical thickness in each. The curve oscillates slightly as conditions change to allow the pilot to peer through each additional protrusion. A third important characteristic, which occurs in this region where a pilot can penetrate multiple protrusions, is that a large increase in $\sigma_o \Delta z$ yields only a minor increase in VCMH. For large $\sigma_o \Delta z$ this corresponds to a pilot's vision penetrating more than one protrusion when the line of sight intercepts only their bottom tips. The fourth characteristic is the area of steep rise between the flat cloud value at large $\sigma_o \Delta z$ and the regions where the oscillations occur. In this area the pilot's view can penetrate only one, or part of

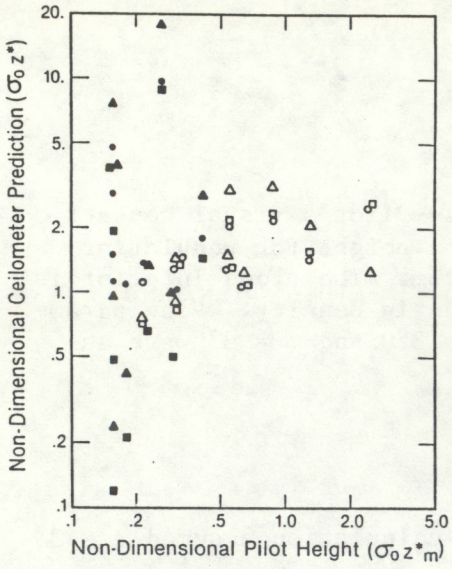

Figure 13.--Average cloud base height from a ceilometer versus pilot visual contact maintenance height for undulating cloud bottom. A variety of protrusion shapes, sizes, and densities are included. Solid symbols denote clouds with homogeneous interior; open symbols denote asymptotical increases of density in the vertical. Squares, triangles, and circles refer to averaging methods 1, 2, and 3, respectively.

one, protrusion. One other important aspect of Fig. 12 is that the VCMH is smaller than $\sigma_o \Delta z$ for all conditions except those in the lower left corner. Therefore, except when the protrusions are small, an airplane is likely to be in clear air part of the time, but the pilot cannot be guaranteed visual contact because of intervening protrusions. The optical density of the protrusions, and their horizontal and vertical dimensions, all effect the height at which a pilot can maintain visual contact.

Since the structure of a nonuniform cloud bottom affects the pilot's ability to hold visual contact, the relationship between a ceilometer signal and the VCMH is important. Figure 13 shows the ratio between VCMH and CBH according to three simple interpretation schemes applied to a variety of cloud conditions. The open symbols represent the cloud model described in (39), which undulates but has a homogeneous interior. The closed symbols represent a cloud whose fringe also undulates sinusoidally, but whose density increases asymptotically above the local fringe.

The scattering coefficient of this second model is expressed mathematically as

$$\sigma = \begin{cases} 0 & z^* < \frac{\Delta z}{2}\,[1 + \cos(2\pi\, x/\Delta x)] \\ \sigma_o[1 - e^{-a\,\sigma_o z^*}] & \text{otherwise .} \end{cases} \qquad (40)$$

The parameters a and σ_o of this latter model were selected such that the optical thickness of a protrusion between $z^* = 0$ and $z^* = \Delta z$ was approximately the same as the undulating homogeneous model. Thus, the asymptotic cloud used $\sigma_o = 0.01\ m^{-1}$ and the homogeneous cloud used $\sigma_o = 0.005\ m^{-1}$. The parameter a was selected such that the optical depth approached the asymptotic value more quickly as Δz decreased. The relationship used was $a = 1.6/\sigma_o \Delta z$.

The criteria for visual contact were again $\phi = 3°$ and $\tau_e = 3.0$. For each of these two cloud types nine combinations of Δx and Δz were selected, which filled a 3 × 3 matrix of conditions. The condition for one side of the matrix was the number of undulations intersected by the pilot's line of sight i.e.; $n = \Delta x \tan\phi/\Delta z$, where $n \simeq 1/4$, 1, and 4. The condition for the orthogonal side of the matrix was governed by the approximate optical depth (3/4, 3, and 12) along the line of sight through one protrusion. The idealized ceilometer in this comparison was a vertically pointing lidar with negligible multiple scattering and infinitely fine spatial resolution. The extinction to backscatter ratio S_L was assumed constant, and $r_L = 1$.

The three methods to interpret the range-corrected ceilometer signals to predict cloud height are:

(1) $\langle H_{max} \rangle$ - Determine the height for maximum signal for each profile, then average these heights

(2) $\langle b_L(z) \rangle_{max}$ - Average the range-corrected signal profiles, then determine the location of the peak

(3) <FOTS> - Determine the height for the FOTS value for each profile, then average these heights. (This gives the same result as averaging the profiles and then finding the height for FOTS).

Averages were taken over one cycle of the undulation.

Figure 13 shows the results, demonstrating poor correlation over the range of conditions examined. All predictors frequently overestimated VCMH, some very seriously. The $\langle H_{max} \rangle$ and $\langle b_L(z) \rangle_{max}$ predictors underestimated VCMH when the optical thickness of each protrusion was small, i.e., less than τ_e. Not only did all three predicters undependably estimate VCMH, but in some of the conditions they were above the height where the pilot could even glimpse the surface at view angle ϕ no matter what his horizontal position. Nature might not frequently generate such a wide range of cloud configurations, so the errors might not be as serious in practice as Fig. 13 indicates. However, these results do show that structure at cloud base can invalidate a criterion for estimating cloud base, even if the criterion is successful for horizontally homogeneous clouds.

In order to interpret ceilometer signals to predict the effect of irregular cloud bottoms, the characteristic horizontal and vertical sizes of the protrusions and their optical density would have to be estimated. An algorithm that handles horizontal inhomogeneity should be based on an empirically confirmed model of protrusion size, shape, and local vertical profiles. However, a successful algorithm would probably utilize a scanning lidar or the short-term history of cloud height from a fixed ceilometer to obtain Δz. The ceilometer could similarly determine Δx by scanning or else by temporal correlation of cloud height and a measurement of wind speed. The FOTS technique, or some simplified derivative thereof, could produce the local vertical profile of optical density. Assuming that the ceilometer signal provides a reasonably faithful representation of cloud presence, progress in signal analysis will probably yield greater improvements in predicting the pilot experience when cloud bottom is variable than will advancements in the sensor alone.

5. SUMMARY

NWS has historically defined cloud base as the height corresponding to the location of maximum RBC signal. This interpretation apparently is based on a simple conceptual model of a homogeneous cloud, which would generate the maximum signal very near the bottom fringe of the cloud. The operational success of the RBC during three decades of service demonstrates that this simple defi-

nition does provide useful information to the aviation industry. The same simple criterion might be applied to signals from lidar ceilometers, to which the NWS may turn for the next generation of instrumentation. An experiment by WPL showed that height for peak RBC signal from non-precipitating clouds agreed within measurement error with the height for peak range-corrected signal from a vertically pointing lidar operating at 694.3 nm wavelength. The peak signal criterion for the RBC, however, has never been proved dependable as an accurate and unbiased predictor of height where a pilot can acquire visual contact with the airport during approach.

The literature provides evidence that the height for peak signal can agree poorly with the visual experience of pilots. During WPL's experiment, the nadir-viewing pilot obtained visual contact with the surface when at the altitude where peak RBC and lidar signal were generated, but had to descend an additional 84 m (275 feet) on average before acquiring visual contact when viewing at 3° depression angle below horizontal without benefit of approach lights. A rather loose physical connection between the factors governing the shape of the ceilometer profile and the pilot's ability to see through obscuring hydrometeors apparently causes the discrepancies. The integrated effect of light scattering along the line of sight degrades the pilot's ability to discern visual cues, while the distribution of scatterers as well as the integrated scatter over a usually different measurement path determine the location of peak ceilometer signal. The research activity on methods for lidar measurement of slant visual range arises from the ceilometer's deficiencies under conditions of very low clouds, fog, or precipitation. Technological advances hold promise for better predictions of the pilot's visual experience.

Improvements in ceilometer measurements can be expected through incorporation of modern optical technology, but more importantly through incorporation of computer technology. Future "smart" ceilometers could acquire more complete and accurate information on the obscurating clouds and precipitation and then properly interpret the available data with more sophisticated algorithms than those currently used. The ceiling measurement function may well merge with efforts to monitor slant visual range. However, any significant improvements in the usefulness of ceilometer outputs must depend on a

correct and adequately detailed understanding of the relationship between the signal profile and the pilot's visual experience.

This relationship between ceilometer and pilot depends on several factors, some of which are as yet unclear. The pilot's ability to see an object depends on its contrast or brightness, the optical depth of the intervening atmosphere, the ambient illumination, and the pilot's physiological response. The ceilometer signal depends on pointing direction, range effects due to optical geometry, spatial resolution, and deviation of wavelength from the visible portion of the spectrum. The vertical distribution of cloud density and the size distribution and thermodynamic phase of the hydrometeors also affect the ceilometer signal. The complex mechanism of multiple scattering can alter the signal, so that it apparently suffers substantially less extinction than for the ideal case of single scattering. A large source of error in current ceilometer practice is probably caused by horizontal inhomogeneity of the cloud bottom. The pilot's ability to see through cloud protrusions depends on their size, shape, and density, for which present operational procedures do not adequately account. More information is needed on vertical and horizontal inhomogeneities at cloud bottom before algorithms can be developed that closely relate the ceilometer signal to the pilot's experience.

The FOTS method for comparing ceilometer signals with the pilot's optical depth solves the equation for the lidar or RBC signal, each of which has two unknowns but only one measurement, by invoking two major but reasonable assumptions. One of these is a large optical depth due to obscuration by hydrometeors along the measurement path. The second assumption is a constant extinction-to-backscatter ratio. Evidence shows that water clouds and precipitation adequately fulfill these assumptions much of the time if the ceilometer wavelength does not deviate too far from the visible. The FOTS technique is a candidate for use as the foundation algorithm in a "smart" ceilometer, and therefore invites further investigation.

6. RECOMMENDATIONS

1) Define optical depth criteria (including accuracy limits) for the pilot, based on aviation operational needs and safety. More than one criterion might be applied, depending on the class of airport operations. During events of low clouds or poor visibility, predicting visual contact with approach lights on instrument approach should assume that the pilot views at some particular angle below horizontal. When cloud bottoms are sufficiently high, recognition of other aircraft by the horizontally viewing pilot while circling might be predicted.

2) Monitor vertical profiles of clouds and their horizontal variability to ascertain the statistical behavior of cloud bottom. Use this information to develop advanced algorithms that relate ceilometer signals to the optical depth criteria, including the important aspects of cloud inhomogeneity.

3) Choose existing or improved optical sensors for the front end of the "smart" ceilometer.

4) Develop algorithms, if needed, to compensate for instrumental limitations, multiple scattering, and differences between the sensor wavelength and the visible.

5) Field test a prototype "smart" ceilometer, which would incorporate a microprocessor to apply the algorithms to the ceilometer signal. Comparison of ceilometer predictions with pilot reports during normal airport operations would be an essential component of the test.

Consumers of outputs from any ceilometer or slant range instrument should be aware of the inherent limitations in accuracy of these devices. No matter how perfect the ceilometer methodology, two important aspects can introduce uncertainty. First are differences among pilots (including the influence of their cockpit environments) in ability to observe their visual cues. Second are the variations in time and space of the density of the cloud bottom, fog, or precipitation. Thus separation in time or space between the aircraft position and the ceilometer's measurement location can introduce uncertainty. Other factors that a practical system may be forced to neglect include the level of ambient illumination and the brightness of the approach lights. The

accuracy of the association between ceilometer and pilot must therefore be described in statistical terms. A ceilometer therefore fulfills a predictive and advisory role, and its measurements should not be considered absolute. It is obvious, however, that devices that better predict the pilot's visual experience can enhance aviation safety and reduce operating costs.

7. ACKNOWLEDGMENTS

V. E. Derr initiated this project, and G. T. McNice, N. L. Abshire, R. E. Cupp, and H. L. Ericson performed the lidar and RBC measurements. M. Kleiman calculated the RBC spectral response. Discussions with J. Bradley, W. Hoehne, and D. George were helpful in formulating the scope of this study.

8. REFERENCES

Carswell, A. I., 1981: Laser measurements in clouds. In Clouds, Their Formation, Optical Properties, and Effects, Academic Press, P. V. Hobbs and A. Deepak, eds., 363-406.

Davis, N. F., 1969: The variation of very low cloud base with time and distance and with height. Meteorol. Mag. 98:351-356.

De Luisi, J. J., B. G. Mendonca, and K. J. Hanson, 1982: Measurements of stratospheric aerosol over Mauna Loa, Hawaii, and Boulder, Colorado. Atmospheric Effects and Potential Climatic Impact of the 1980 Eruptions of Mount St. Helens, NASA Conference Publication 2240, pp. 117-123. [NTIS N83-11534/5].

Deirmendjian, D., 1969: Electromagnetic Scattering on Spherical Polydispersions. Elsevier, 290 pp.

Derr, V. E., 1980: Estimation of the extinction coefficient of clouds from multi-wavelength lidar backscatter measurements. Appl. Opt. 19:2310-2314.

Derr, V. E., N. L. Abshire, R. E. Cupp, and G. T. McNice, 1976: Depolarization of lidar returns from virga and source cloud. J. Appl. Meteorol. 15:1200-1203.

Eberhard, W. L., V. E. Derr, and M. Kleiman, 1980: Comparison of ceiling as determined by lidar, other ceilometers, and pilot slant visual range. Conference Abstracts Tenth International Laser Radar Conference, Silver Spring, Maryland, Amer. Meteor. Soc., p. 38.

Eberhard, W. L., 1983: Eye-safe tracking of oil fog plumes by UV lidar. Appl. Opt. 22:2282-2285.

Eggert, W. E., 1960: Approach visibility studies at Newark, final report. AMB Project D-1-902, Bureau of Research and Development, Federal Aviation Agency, 112 pp. [NTIS AD262769].

Gaumet, J. L., and A. Petitpa, 1982: Lidar-transmissometer visibility comparisons over slant and horizontal paths. J. Appl. Meteorol. 21:683-694.

Gudiksen, P. H., G. J. Ferber, M. M. Fowler, W. L. Eberhard, M. A. Fosberg, and W. R. Knuth, 1984: Field studies of transport and dispersion of atmospheric tracers in nocturnal drainage flows. Atmos. Environ. 18:713-731.

Khrgian, A. K., 1963: Cloud Physics. Israel Program for Scientific Translations, 392 pp.

Kohl, R. H., 1977: New lidar concept for measuring the slant range transmission in aircraft landing approaches. Conference Abstracts, 8th International Laser Radar Conference, Philadelphia, Amer. Meteor. Soc.

Kohl, R. H., 1978: Discussion of the interpretation problem encountered in single-wavelength lidar transmissometers. J. Appl. Meteor. 17:1034-1038.

Lopez, R. E., 1977: Some properties of convective plume and small fair-weather cumulus fields as measured by acoustic and lidar sounders. J. Appl. Meteorol. 16:861-865.

Middleton, W. E. K., 1952: Vision through the Atmosphere. Univ. of Toronto Press, 250 pp.

Noonkester, V. R., 1984: Droplet spectra observed in marine stratus cloud layers. J. Atmos. Sci. 41:829-845.

Pinnick, R. G., S. G. Jennings, P. Chylek, C. Ham, and W. T. Grandy, Jr., 1983: Backscatter and extinction in water clouds. J. Geophys. Res. 88:6787-6796.

Plass, G. N., and G. W. Kattawar, 1971: Reflection of light pulses from clouds. Appl. Opt. 10:2304-2310.

Platt, C. M. R., 1973: Lidar and radiometric observations of cirrus clouds. J. Atmos. Sci. 30:1191-1204.

Platt, C. M. R., N. L. Abshire, and G. T. McNice, 1978: Some microphysical properties of an ice cloud from lidar observation of horizontally oriented ice crystals. J. Appl. Meteorol. 17:1220-1224.

Platt, C. M. R., 1981: Transmission and reflectivity of ice clouds by active probing. In Clouds, Their Formation, Optical Properties, and Effects, Academic Press, P. V. Hobbs and A. Deepak, ed., 407-435.

Platt, C. M. R., and A. C. Dilley, 1984: Determination of the cirrus particle single-scattering phase function from lidar and solar radiometric data. Appl. Opt. 23:380-386.

Rotating Beam Ceilometer System Instruction Manual, 1967: WB 1082 USCOMM-ESSA-DC, Engineering Div., U.S. Dept. of Commerce, Silver Spring, Maryland.

Sassen, K., and K. Liou, 1979: Scattering of polarized laser light by water droplet, mixed-phase and ice crystal clouds. Part II: Angular depolarizing and multiple-scattering behavior. J. Atmos. Sci. 39:852-861.

Shipley, S. T., and J. A. Weinman, 1978: A numerical study of scattering by large dielectric spheres. J. Opt. Soc. Am. 68:130-134.

Viezee, W., E. E. Uthe, and R. T. H. Collis, 1969: Lidar observations of airfield approach conditions, an exploratory study. J. Appl. Meteorol. 8:274-283.

Weinman, J. A., 1976: Effects of multiple scattering on light pulses reflected by turbid atmospheres. J. Atmos. Sci. 33:1763-1771.

Wendling, P., R. Wendling, and H. Weickmann, 1979: Scattering of solar radiation by hexagonal ice crystals. Appl. Opt. 18:2663-2671.

Zuev, V. E., 1982: Laser Beams in the Atmosphere. Consultants Bureau, Plenum Publishing, 504 pp.

APPENDIX

An approximate, analytical form of $F_R(\theta_R)$ for $\theta_R \lesssim 85°$ is developed here by assuming that the RBC operates in a diffuse, homogeneous field of scatterers. The volume filled by the RBC beam is approximately a trapezoidal pyramid with the vertex at the transmitter. The flux density of the light is considered uniform over the rectangular area formed by a plane that intersects the pyramid normal to the center line of propagation. The flux density E at a distance x from the transmitter is

$$E = \frac{P}{(x\ \psi_{tp})(x\ \psi_{th})} \quad , \tag{A1}$$

where P is the beam power, ψ_{tp} is the full angle of the trapezoidal pyramid in the vertical plane, and ψ_{th} is the full angle in the horizontal (see Fig. A1). The small angle approximation $\tan\varepsilon \simeq \varepsilon$ was used. The receiver's field of view is considered an inverted trapezoidal pyramid with vertex at the receiver. The sensitivity over this field at any particular height H is assumed uniform. The angles ψ_{rp} (in the plane containing the transmitter) and ψ_{rh} characterize the full angles that define the field of view.

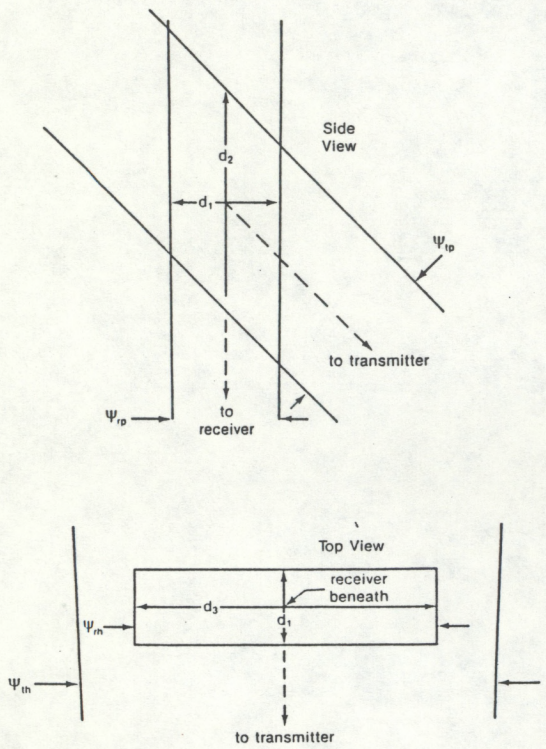

Figure A1.--Geometry of the RBC's volume of intersection between transmitter and receiver.

The energy reaching the detector is

$$P_R = E\ \beta_R(\theta_R)\ V\ \Omega\ , \tag{A2}$$

where $\beta_R(\theta_R)$ is the scattering coefficient for RBC angle θ_R, V is the volume of intersection of the two pyramids, and $\Omega = A/H^2$ is the solid angle subtended by the receiver aperture of area A as measured from the center of the volume at height H above. The intersection volume has approximate dimensions

$$d_1 = H\ \psi_{rp}/\cos\theta_R \tag{A3}$$

$$d_2 = \ell\ \psi_{tp}/\cos\theta_R\ . \tag{A4}$$

The third dimension separates into two regions. The width of the transmitted beam is

$$d_{3t} = \ell\ \psi_{th}/\cos\theta_R, \tag{A5}$$

and the width of the receiver's field of view is

$$d_{3r} = \ell\ \psi_{rh}/\tan\theta_R\ . \tag{A6}$$

Thus

$$d_3 = \begin{cases} H\ \psi_{rh} & \text{if } \theta_R < \theta_R' \\ \ell\ \psi_{th}/\cos\theta_R & \text{if } \theta_R > \theta_R'\ , \end{cases} \tag{A7}$$

where

$$\theta_R' = \sin^{-1}\ (\psi_{th}/\psi_{rh})\ . \tag{A8}$$

If the honeycomb were removed, θ_R' would be about 43°; with it installed θ_R' is roughly 90°. Since $V = d_1 \times d_2 \times d_3$, the RBC sensitivity reduces to

$$P_R(\theta_R < \theta_R') = \frac{PA\beta_R(\theta_R)}{\ell} \frac{\psi_{rp}\ \psi_{rh}}{\psi_{th}} \tag{A9}$$

$$P_R(\theta_R' < \theta_R \lesssim 85°) = \frac{PA\beta_R(\theta_R)}{\ell} \frac{\psi_{rp}}{\sin\theta_R} \quad . \tag{A10}$$

The simple geometrical description in this analysis breaks down as $\theta_R \to 90°$ (as does the accuracy of the RBC), hence the restriction of $\theta_R \lesssim 85°$.

The noteworthy aspect of this result is the weak [in Eq. (A9)] or missing [in Eq. (A10)] dependence of received power on RBC angle θ_R. Although the intersecting volume becomes more distant from the receiver as θ_R increases, which tends to reduce the sensitivity, the size of the volume grows at a compensating rate when $\theta_R < \theta'_R$. When $\theta_R > \theta_R'$ the decrease in sensitivity with larger θ_R is very gradual.

If the optical depth that is traversed by RBC radiation between entry and exit from the intersecting volume becomes significant, the assumption of a diffuse scattering medium is no longer valid. The increasing size of the scattering volume can no longer fully compensate for the increasing distance to the receiver. In the limit of large optical depth through the intersecting volume, the RBC sensitivity approaches an H^{-2} dependence.